Journal of Power Sources 645 (2025) 237120

Contents lists available at ScienceDirect

Journal of Power Sources

journal homepage: www.elsevier.com/locate/jpowsour

Determination of temperature distribution of a solid oxide cell stack using regenerated fiber Bragg gratings

Shengzhi Liang [a,b,*], Qiang Bian [c], Dominik Schäfer [a], Johannes Roths [c], Rüdiger-A. Eichel [a,b,d]

[a] Forschungszentrum Jülich GmbH, Institute of Energy Technologies, Fundamental Electrochemistry (IET-1), Jülich, D-52425, Germany
[b] RWTH Aachen University, Institute of Physical Chemistry, Aachen, D-52074, Germany
[c] Munich University of Applied Sciences, Photonics Laboratory, Munich, D-80335, Germany
[d] RWTH Aachen University, Faculty of Mechanical Engineering, Aachen, D-52062, Germany

GRAPHICAL ABSTRACT

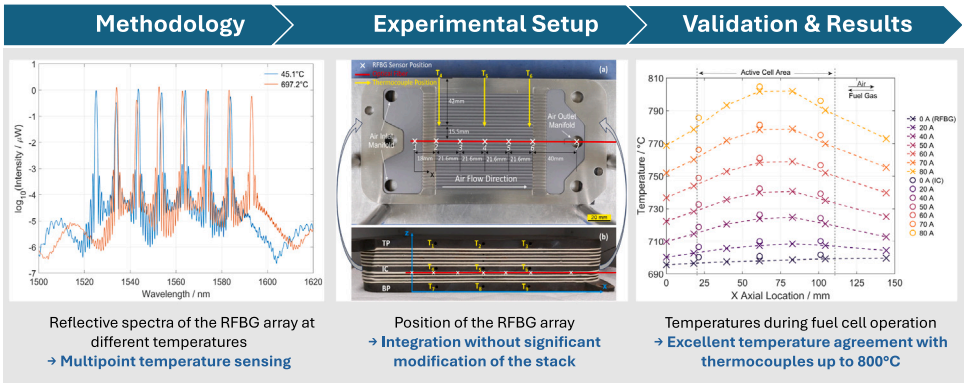

HIGHLIGHTS

- RFBG sensors conduct multipoint temperature measurement in a SOC stack.
- Asynchronous heating of the stack caused thermal gradient during heat up.
- RFBG sensors are more suitable for capturing transient temperature changes.
- Significant temperature change during IV curve leads to incorrect estimation of ASR.
- Heat conduction dominates the heat dissipation during fuel cell operation.

ARTICLE INFO

Keywords:
Solid oxide cell stack
Regenerated fiber bragg grating
Temperature distribution
Thermal gradient
Energy balance

ABSTRACT

The temperature distributions inside the solid oxide cell (SOC) stacks are conventionally monitored using thermocouples. Despite their reliability, employing a large number of thermocouples is often not practical due to their electrical conductivity and significant cabling effort. In this work, an optical fiber with an array of seven regenerated fiber Bragg grating (RFBG) sensors was integrated into a modified Jülich F10 solid oxide cell stack to address these challenges. The transient temperature profiles during heat-up and current–voltage characterization, as well as the steady state profiles during fuel cell operation under varying conditions were

* Corresponding author at: Forschungszentrum Jülich GmbH, Institute of Energy Technologies, Fundamental Electrochemistry (IET-1), Jülich, D-52425, Germany.
E-mail address: s.liang@fz-juelich.de (S. Liang).

https://doi.org/10.1016/j.jpowsour.2025.237120
Received 24 February 2025; Received in revised form 12 April 2025; Accepted 17 April 2025
Available online 2 May 2025

recorded using both the RFBG sensors and nine type-N thermocouples. The RFBG sensors provided accurate, localized temperature measurement up to 800 °C in the stack. Based on the recorded temperature profiles, the underlying causes for thermal gradient and heat dissipation of this five-layer SOC stack were analyzed and stack operating strategies were discussed. This study demonstrated the feasibility and advantages of using RFBG sensors in SOC applications and established previously inaccessible boundary conditions for stack level simulation work.

1. Introduction

Solid oxide cells (SOCs) are regarded as a promising technology for the sustainable energy transition thanks to their high efficiency, low emission profile, multifuel and reversible operation capabilities [1–4]. Despite extensive studies and significant advancement in SOC technology over the past decades, the commercialization of SOC remains constrained by its high degradation rate and manufacturing cost. The state-of-the-art SOC stack at Forschungszentrum Jülich exhibited a voltage degradation rate of approximately 0.6% kh^{-1} in the first 10,000 h of fuel cell operation at a current density of 1 A cm^{-2} and 80% fuel utilization [5], while the U.S. Department of Energy set the goal of 0.2% kh^{-1} with at least 40,000 h of lifetime [6]. To bridge the gap between the current and the targeted long-term performance and stability of the SOC stack, a comprehensive understanding of the degradation mechanisms is essential.

The degradation of the SOC stack is a complex process that involves multiple mechanisms [7] simultaneously. A great number of researches have been dedicated to identify and clarify these mechanisms [5,8–14]. Among these, the thermally induced degradation mechanisms are of particular interest. On the one hand, prolonged exposure to high operating temperature and the formation of local hot spots can accelerate the thermochemical related degradation due to the enhanced kinetics. On the other hand, thermomechanical stresses arise from the mismatch in the coefficient of thermal expansion (CTE) of adjacent components and thermal gradients can damage various stack components and lead to premature stack failure [15–17]. To address the issues of local hot spots and thermal stress distributions in the stack, an in-depth investigation of the temperature profile in the stack is imperative.

Despite extensive efforts to study the temperature distribution in SOC stacks, the availability of published experimental data remains very scarce, especially at a higher spatial resolution. Among different temperature sensing techniques, thermocouples are most prevalent thanks to their high accuracy, temperature resistance, and relatively low cost. Razbani et al. [18] employed five type-K thermocouples to monitor the temperature distribution across the middle cell of a six-layer SOFC stack with cross flow configuration. Celik et al. [19] mounted thermocouples to the metal interconnect using adhesive to investigate the temperature distribution of a relatively large short stack (cell area 81 cm^2) under different flow types and loads. Similarly, Fang et al. [20] used multiple thermocouples in an 18-layer Jülich F20 stack operating with both hydrogen and simulated reformate as fuels to record the temperature distribution under various operating conditions.

Although the conventional thermocouples are well established for temperature measurement, obtaining the temperature distribution of the stack with high spatial resolution still remains a practical challenge. Since each thermocouple conducts only a single-point measurement, achieving a high spatial resolution necessitates the use of a large number of thermocouples, which introduces several drawbacks. Firstly, the electrical conductivity of the thermocouples presents a short-circuit hazard, especially when used in high spatial density. Secondly, the insertion of the thermocouples could compromise the gas tightness of the stack [21]. Additionally, thermocouples themselves act as heat conductors, leading to extra heat loss to the system. To address these issues, Ranaweera et al. [22] and Guk et al. [23–25] developed a multi-junction thermocouple array for temperature sensing directly on the electrode. They achieved a higher spatial and temporal resolution compared to the conventional approach.

Thermal imaging is another powerful tool for achieving both high spatial and temporal resolution in temperature measurements [26–28]. However, the applicability of thermal imaging is so far strongly limited to single cell testing, as there is no practical way to capture the thermal image of active cell area inside the stack. Optical fiber sensors (OFSs) are well known for their compact size, high spatial and temporal resolution, inherent immunity to electromagnetic interference, low thermal inertia and conductivity [29,30]. Yan et al. [31] developed distributed optical fiber sensors based on Rayleigh back scattering profiles to study the real-time temperature profiles of solid oxide fuel cells (SOFC). The sensors demonstrated promising performance in the hydrogen loaded atmosphere at temperatures up to 800 °C, with a spatial resolution of 5 mm.

In addition to the distributed OFSs, fiber Bragg gratings (FBGs) have received significant attention in recent years for high temperature sensing due to their design flexibility and high measurement accuracy. Among the various types of FBGs developed, regenerated fiber Bragg gratings (RFBG), which are fabricated by a thermal annealing process, demonstrate excellent performance for accurate, reliable and multi-point high-temperature sensing [32]. In a recent work [33], the authors proposed a straightforward calibration method for RFBG sensors used for temperature sensing up to 700 °C. The uncertainty of the sensor within its calibration range was found to be in compliance with the European standard IEC 60584 for non-calibrated thermocouples. Readers are referred to Refs. [32,34–38] for more details on the FBG as temperature sensors.

In this work, a Jülich F10 SOC stack was modified to incorporate an optical fiber with an array of seven RFBG sensors to record the temperature distribution along a stack layer. The temperature profiles of the stack were investigated using the RFBG sensors in conjunction with nine type-N thermocouples during heat-up, current–voltage curve measurements and steady state fuel cell operation with varying air flow rates and loadings.

2. Experimental

2.1. SOC stack preparation and sensors integration

A five-layer Jülich F10 SOFC stack was used for the present study. The fuel electrode supported solid oxide cells (Elcogen, Estonia) in the stack comprised Ni-8YSZ (8 mol% yttria-stabilized zirconia) fuel electrodes, 8YSZ electrolytes and LSC ($La_{0.6}Sr_{0.4}CoO_{3-\delta}$) air electrodes with an in-house screen-printed LSCF ($La_{0.58}Sr_{0.4}Co_{0.2}Fe_{0.8}O_{3-\delta}$) contact layer. The cells had dimensions of 10 cm × 10 cm with an active cell area of 80 cm^2. The interconnects and cell frames were made from Crofer 22 APU, and an MCF ($MnCo_{1.9}Fe_{0.1}O_4$) protective coating was applied to the surfaces in the air compartments by atmospheric plasma spraying. The fuel gas and air flowed through each stack layer in a counterflow configuration. A stainless-steel guiding tube with an outer diameter of 1 mm and 0.2 mm wall thickness was introduced in the middle air channel on the second stack layer (counting from the bottom), as depicted in Fig. 1, to guide the installation of the optical fiber to the desired position and minimize the influence of gas leakage.

The stack was joined at a different test rig following our in-house standard joining procedure. The fuel compartment was flushed with argon at 2.50 L min^{-1} and the air compartment with air at 2.50 L min^{-1} (all volumetric flow rates reported in this work are referenced to the conditions of 273.15 K and 101.325 kPa). The stack temperature was gradually increased to 850 °C and held for 100 h while applying

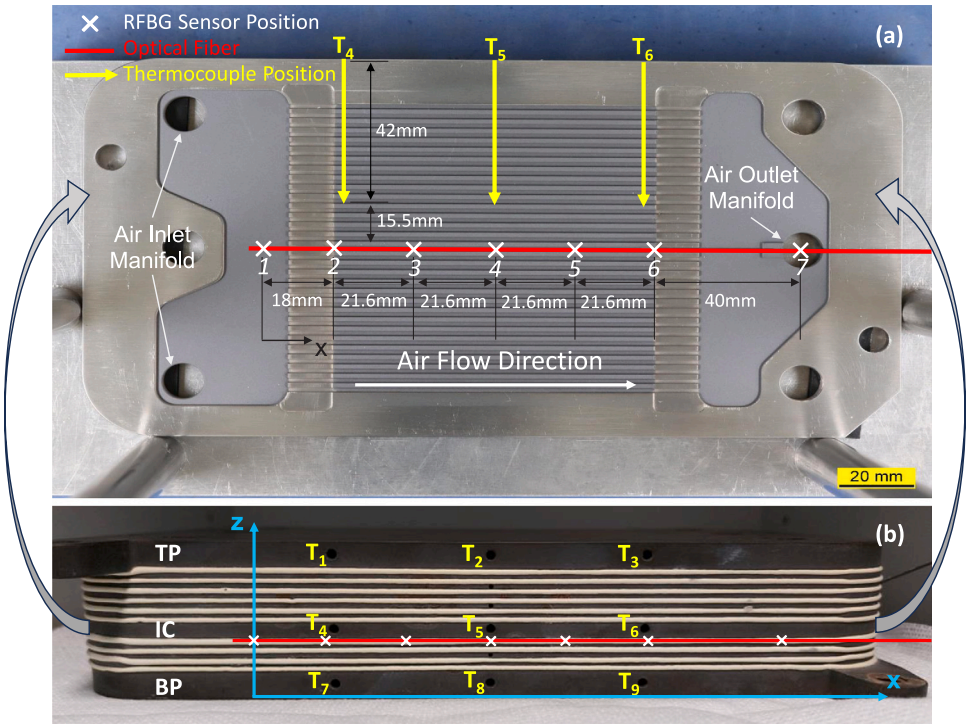

Fig. 1. Positions of RFBG sensors and type-N thermocouples in the stack with respect to (a) the interconnect in the middle of the stack and (b) the frontal view. (TP: top cover plate, IC: middle interconnect, BP: bottom cover plate).

a constant clamping force of 1 kN to allow the crystallization of the glass sealant. After joining, the stack was cooled to room temperature and integrated into a hot-box test rig with the fuel electrode side facing downwards. In this hot-box test rig, the gases and deionized water were supplied by mass flow controllers that were carefully calibrated prior to the stack testing. The stack was sandwiched between two heating plates equipped with integrated heating cartridges for temperature control. An additional adapter plate was used to connect the gas inlets of the stack to the heating plate in the bottom, as the test rig was originally built for a different stack design. To minimize heat loss, the stack and the heating plates were insulated by a 10 cm thick layer of microporous thermal insulation and an additional 2 cm layer of glass wool. For the reduction of the Ni-YSZ fuel electrodes, the stack temperature was adjusted to 800 °C with an initial flow of 2.50 L min^{-1} argon and 2.50 L min^{-1} air followed by a step-wise increase of H_2 concentration in the fuel gas mixture up to 56 mol%. Similar joining and reduction procedures for the Jülich F10 stack were reported elsewhere [9,39,40]. After reduction, the operational integrity and electrochemical performance of the stack was checked using the current–voltage (IV) characterization and electrochemical impedance spectroscopy (EIS) before the stack was cooled to room temperature for the safe insertion of the optical fiber. All reported EIS measurements were performed with 20.00 L min^{-1} air and 5.56 L min^{-1} H_2, while IV curves were measured with an addition of 20 mol% steam (1.39 L min^{-1}) blended into the fuel gas mixture unless stated otherwise. During the IV characterizations, the current was ramped up in increments of 2 A every six seconds until it reached the targeted value, or the voltage of any cell dropped below 620 mV. Afterward, the current was reduced to zero at the same rate, yet only the first half of the IV curve (current increasing) was visualized and evaluated for electrochemical performance. The EIS measurements were conducted using a PP211 potentiostat and IM6 electrochemical workstation (Zahner-Elektrik GmbH, Germany) at a direct current of 5 A with an alternating current amplitude of 2 A, and covered the frequency range from 0.1 Hz to 20 kHz. The accuracy of the nine type-N thermocouples was verified at 600 °C, 700 °C and 800 °C using a Pegasus 4853 S dry block calibration oven (Isothermal Technology Limited, UK) equipped with a high-precision type-R reference thermocouple (Klasmeier GmbH, Germany). After the inspection, the thermocouples were positioned in the 42 mm deep thermocouple wells of the top cover plate (TP), interconnect (IC), and bottom cover plate (BP). The optical fiber with the RFBG sensor array was carefully slid into the stainless-steel guiding tube and fixed at the desired depth. The positions of the thermocouples and the RFBG sensors are shown in Fig. 1.

After successfully inserting the optical fiber, the stack was heated again with 5.00 L min^{-1} forming gas (4 mol% H_2 and 96 mol% Ar) and 5.00 L min^{-1} air at a rate of 2 K per minute. The stack performance was assessed again using the same electrochemical techniques and operating conditions to evaluate the impact of the fiber. For fuel cell operation under constant load, the stack was supplied with 3.50 L min^{-1} H_2 and 8.30 L min^{-1} air.

2.2. RFBG sensors and data evaluation

To prepare the RFBG sensors, seven seed gratings with wavelengths ranging from 1525 nm to 1585 nm were inscribed into a hydrogenated single-mode fiber using a KrF excimer laser by phase mask method. Each grating was 0.9 mm in length. Following a 30-h hydrogen out-diffusion process at 80 °C, these seed gratings were annealed at 800 °C for 65 h to complete the regeneration process. Fig. 1 depicts the positions of the resulting RFBGs (white cross symbols) along the optical fiber (red line).

It was observed that the temperature-induced Bragg wavelength changes of all RFBGs fabricated on the same type of fiber following the same regeneration and annealing process exhibited consistent behavior, i.e., similar temperature sensitivity [36]. For RFBGs with large wavelength range (1525–1585 nm), a generalized and wavelength-dependent temperature calibration function was preferred to achieve high accuracy temperature measurement. This calibration function can be expressed as follows [33]:

$$\lambda_B(T, \lambda_{cal}) = \lambda_{cal}\left[1 + \sum_{i=1}^{4} \bar{B}_i T_{cal}^{i}\right]^{-1}\left[1 + \sum_{i=1}^{4} \bar{B}_i T^{i}\right] \quad (1)$$

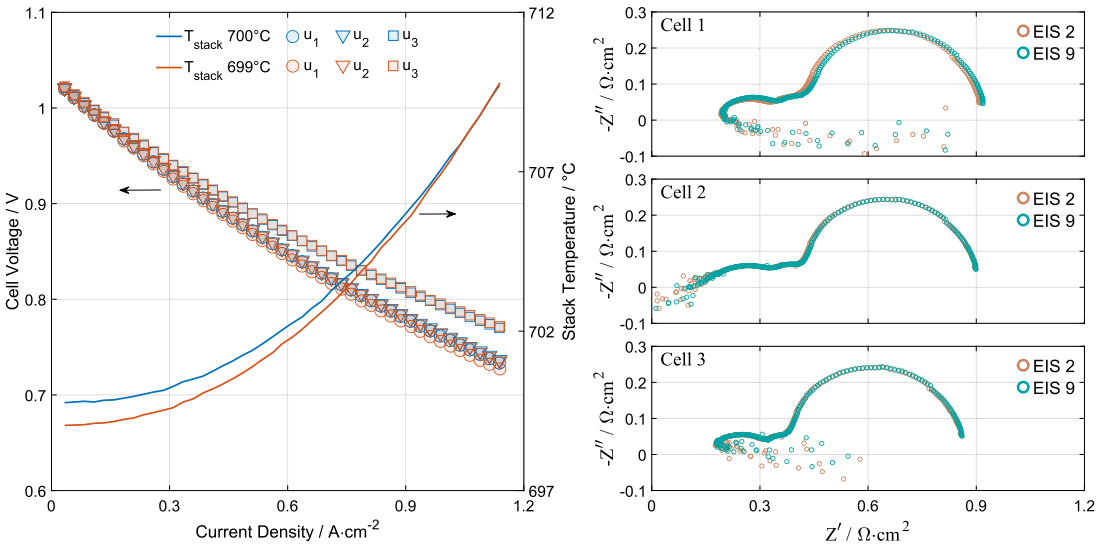

Fig. 2. Left: Current voltage characteristics of cell 1 (circle), 2 (triangle) and 3 (square) measured at 700 °C with 5.56 L min^{-1} H_2 and 1.39 L min^{-1} steam as fuel and 20.00 L min^{-1} air, with (red) and without (blue) fiber. Both sets of measurements reached the maximal current density of 1.125 A cm^{-2}. Right: EIS spectra of cell 1, 2 and 3 measured at 700 °C with 5.56 L min^{-1} H_2 and 20.00 L min^{-1} air, with (EIS 9) and without the fiber (EIS 2).

where λ_B is the measured Bragg wavelength of the RFBG sensor, λ_{cal} is the offset wavelength at the calibration temperature T_{cal}, and $\bar{B}_i$ are the generic wavelength-normalized calibration coefficients. The values of these parameters, the spectral response and the temperature sensitivities of the RFBG sensors used in this work can be found in the supplementary material S1.

The optical fiber was protected by a quartz capillary with an outer diameter of 0.435 mm. The reflection spectrum of the optical fiber during both calibration and stack testing was captured by a si255 optical sensing interrogator (Micron Optics Inc., USA). The si255 features an internal depolarizer and the Bragg wavelength of each RFBG sensors was determined using a peak seeking algorithm developed by the Photonics Laboratory (Munich University of Applied Sciences, Germany). The sampling rate for the Bragg wavelengths were 0.1 Hz, 1 Hz and 0.05 Hz during the heat-up, current–voltage curve measurement and steady state fuel cell operation, respectively. The temperatures corresponding to the Bragg wavelengths were calculated by numerically inverting the generalized wavelength-dependent calibration function given in Eq. (1).

Due to the differing sampling rates of the RFBG sensors and thermocouples, the temperature data in this study were processed as follows: During steady-state operation, the arithmetic mean value was calculated using eleven consecutive thermocouple readings collected over five minutes. For each thermocouple reading, the temporally nearest RFBG sensor reading was selected, and the arithmetic mean of these selected RFBG readings was then calculated. In contrast, during transient operation, the temporally nearest RFBG and thermocouple readings at the specific timestamp were directly evaluated without averaging.

3. Results and discussion

3.1. Electrochemical performance

The primary concern with introducing a stainless steel guiding tube into the air compartment of the stack is the risk of short circuit, as the tube could compromise the electrical isolation provided by the glass sealant between the interconnect and the adjacent cell frame. Therefore, the open circuit voltage (OCV) of cell 2, where the guiding tube was installed, was immediately checked after the reduction for any signs of short circuit or severe gas cross-over. At 700 °C, with 5.56 L min^{-1} pure H_2 and 20.00 L min^{-1} air, the OCV of cell 2 at 700 °C was 1.218 V, which was in good agreement with the average OCV of all five layers at 1.211 V. Based on the voltage, the molar fraction of steam in the fuel gas compartment can be calculated using the Nernst equation:

$$E_{cell} = E^0_{cell}(T) + \frac{RT}{zF} \ln\left(\frac{a_{H_2O,anode}}{a_{H_2,anode} \cdot a^{0.5}_{O_2,cathode}}\right) \quad (2)$$

where E_{cell} is the cell potential, E^0_{cell} (T) the standard cell potential at temperature T, R is the universal gas constant, z is the number of charge transferred, F is the Faraday constant, and a is the activity of the respective species, which can be substituted by their partial pressures in this case. Using the average voltage value, this equation yields a steam molar fraction of 0.3 mol% in the fuel gas compartment. Following the completion of the present work, the same stack was integrated into a different test rig, where the cell 2 and the average cell voltage were found to be 1.280 V and 1.265 V under the same conditions. For this case, the average cell voltage corresponded to a 0.09 mol% of steam. The higher fraction of steam observed in the present work suggested a minor external leakage between the test rig and the stack, likely caused by the gaskets between the adapter plate and the bottom cover plate. More importantly, the introduction of the guiding tube did not result in a short circuit or significant gas cross-over in this stack layer.

Fig. 2 illustrates the current voltage characteristics of cell 1, 2 (where the fiber was placed), and 3, as well as the development of the average stack temperature during the measurements conducted after reduction with (red) and without (blue) the fiber. Cell 4 and 5, which were nonadjacent to cell 2, are not shown here for the sake of simplicity. The performance of cell 2 showed no significant deviation from cell 1, yet slightly worse than that of cell 3. This difference was likely caused by the more pronounced temperature elevation in the middle of the stack during polarization, which will be articulated in detail in Section 3.3. Furthermore, the characteristic curves of each cell, with and without fiber, mostly overlapped, and the performance was in line with other F10 stacks tested at Forschungszentrum Jülich [39–41]. The Nyquist plots show the EIS spectra of the same cells, recorded on the same day as the polarization curves. Due to the poor data quality in the high frequency region, the ohmic resistance of each cell cannot be extracted accurately. However, the total polarization resistances of cell 1 and cell 2 were nearly identical, while cell 3 performed only marginally better, which can also be attributed to the temperature effect. In summary, the introduction of the guiding tube and the optical fiber on the air side of one cell had no noticeable impact on the cell performance, confirming the stack's readiness for further testing.

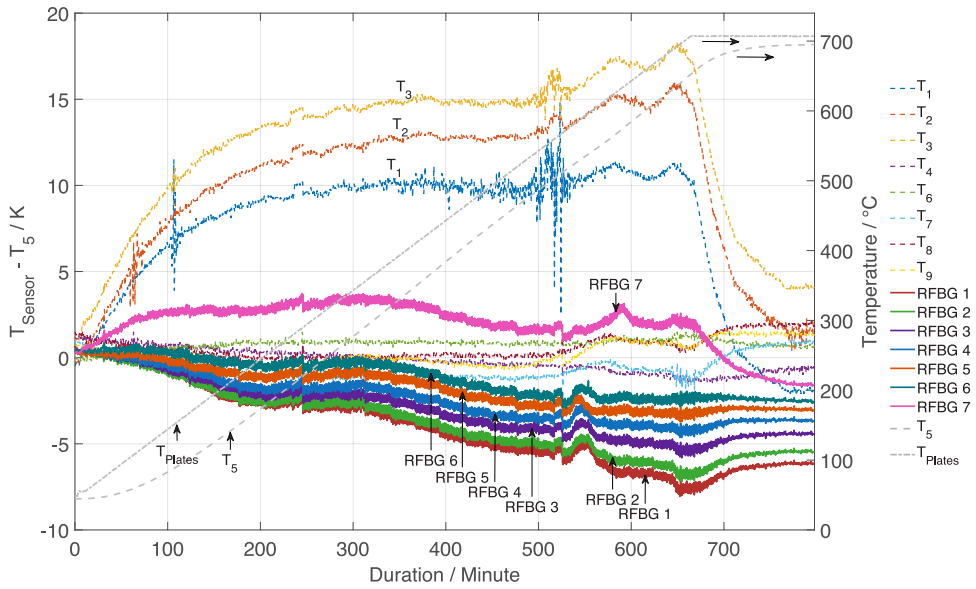

Fig. 3. The development of the temperature differences between various temperature sensors and T_5 (plotted on the left vertical axis) alongside the average temperature of the heating plates and T_5 (plotted on the right vertical axis) over the duration of the heat-up process of the SOC stack at the rate of 1 K min^{-1}.

3.2. Temperature development during heat-up

In Fig. 3, the temperature differences between T_5 (measured by the type-N thermocouple located in the center of the stack, see Fig. 1) and the seven RFBG sensors along with the remaining eight thermocouples are plotted on the left vertical axis. The mean temperature of two heating plates and the absolute temperature of T_5 are plotted on the right vertical axis over the duration of the heat-up process. The set temperatures of both heating plates were increased by 1 K per minute.

At room temperature, all RFBG sensors and thermocouples deviated less than 2 K from T_5. This is as expected as the calibration of the RFBG sensors was performed at room temperature. Starting from 120 min into the heat-up process, T_5 exhibited a linear increase until the temperature difference between it and the heating plates started to diminish at around 650 min. During this linear phase, the temperature curves of T_5 and the heating plate were visually parallel, suggesting an almost constant temperature difference between them. Apart from the sensors T_1, T_2, and T_3, the temperature differences of all other sensors and T_5 remained within 7 K throughout the entire heating process. These three thermocouples were located in the top cover plate (TP), which was separated from the upper heating plate only by one layer of Mica gaskets. The bottom cover plate (BP), however, was mounted on an adapter plate that connected the gas inlet manifolds of the stack to the lower heating plate, since this test rig was initially designed for a different stack manifold configuration. Due to the significant thermal inertia of the adapter plate, the temperature of the BP always lagged behind the TP during the heat-up process. Consequently, the fuel gas and air should also be cooler than the TP but closer in temperature to the BP, as they passed through the adapter plate before entering the stack.

Additionally, the RFBG sensors registered a slight increase in temperature from the air inlet to the outlet side of the stack (RFBG 1 < RFBG 2 < ... < RFBG 7). A similar tendency was also observed with T_1, T_2, and T_3, confirming the cooling effect of the air. Interestingly, this effect was not seen for the thermocouples in the middle interconnect and the bottom cover plate, indicating that their temperatures were closer to the air temperature in comparison to the top cover plate.

At around 530 min, T_1, T_2 and T_3 exhibited different extents of fluctuation, whereas T_5 remained on the linear trajectory, and the rest of the thermocouples showed only minor change in deviation from T_5. Notably, all RFBG sensors, which were directly exposed to air flow, also registered a subtle temperature fluctuation, indicating a genuine variation in temperature rather than electromagnetic interference. Unfortunately, the data from the test rig was only logged every thirty seconds, and no noticeable abnormalities, besides the temperatures, were recorded in the raw data. One possible rationale for this fluctuation could be a non-ideal tuning of the electrical heating. In the final stage of the process, once the heating plates reached the desired setpoints, the temperatures of the top cover plate and other layers quickly converged. After stabilization, the temperatures measured by RFBG 2, 4 and 6 were compared with the closest thermocouples T_4, T_5 and T_6 to verify the their accuracy. The results are listed in Table 1.

Table 1
Average temperatures over a five minutes period at the end of the heat-up process after stabilization, standard deviation is provided as uncertainties.

Sensors	RFBG/°C	Thermocouple/°C
RFBG 2 & T_4	690.78 ± 0.03	695.70 ± 0.04
RFBG 4 & T_5	692.43 ± 0.02	696.26 ± 0.05
RFBG 6 & T_6	693.67 ± 0.01	696.96 ± 0.08

In general, the temperature deviations between the adjacent sensors were all within 5 K. While the readings of RFBG sensors were slightly lower than their nearest thermocouple counterparts, particularly in the upstream region of the air flow, the discrepancy can be attributed to the differing sensor placements (see Fig. 1(a)) and the direct exposure of the RFBG sensors to air flow. Notwithstanding, the differences were all marginal, and the close agreement in temperature measurement confirmed the accuracy and reliability of the RFBG sensors up to 700 °C.

To better visualize and analyze the temperature distribution in the stack, the thermal gradient profile at the moment when T_5 reached 500 °C is shown in Fig. 4(a). The thermal gradients, defined as $\nabla T = (\partial T/\partial x, \partial T/\partial z)$, are calculated using the "gradient" function in MATLAB [42] based on the readings from nine thermocouples. The diagram depicts the thermal gradients at their corresponding sensor positions from the frontal perspective of the stack, as shown in Fig. 1(b). Notably, the top cover plate exhibited the most noticeable thermal gradient, followed by the interconnect in the middle and bottom cover plate. The arrows predominantly pointed vertically upward, indicating that the vertical thermal gradient across different layers was more pronounced than the horizontal thermal gradient within one layer. It is

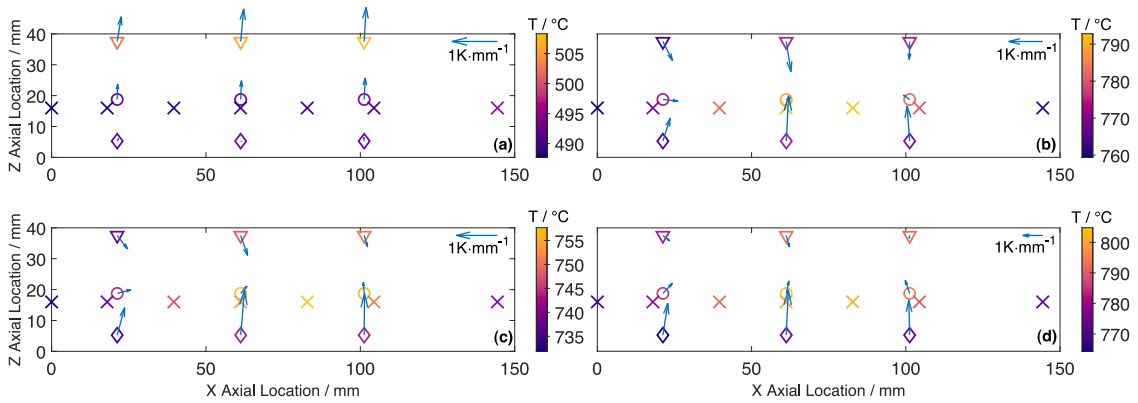

Fig. 4. The thermal gradient profiles of the stack determined based on the temperature readings from nine type-N thermocouples. The direction and the length of the arrows indicate the direction and the magnitude of the local thermal gradient, while the color of the symbols represents the temperature measured at the corresponding positions (Triangles: temperatures measured by the thermocouples T_1, T_2, T_3 in the top cover plate; Circles: T_4, T_5, T_6 in middle interconnect, diamonds: T_7, T_8, T_9 in bottom cover plate, Crosses: temperatures measured by RFBG sensors 1 to 7). Note the difference in color bar and thermal gradient scale across each diagram. The thermal gradient profiles are presented for the following conditions: (a) when T_5 = 500 °C during the heat-up process; (b) at 600 s during the polarization curve measurement; (c) during steady state fuel cell operation at 60 A (0.75 A cm^{-2}) with 20.00 L min^{-1} air flow; (d) during steady state fuel cell operation at 80 A (1.00 A cm^{-2}) with 8.30 L min^{-1} air flow.

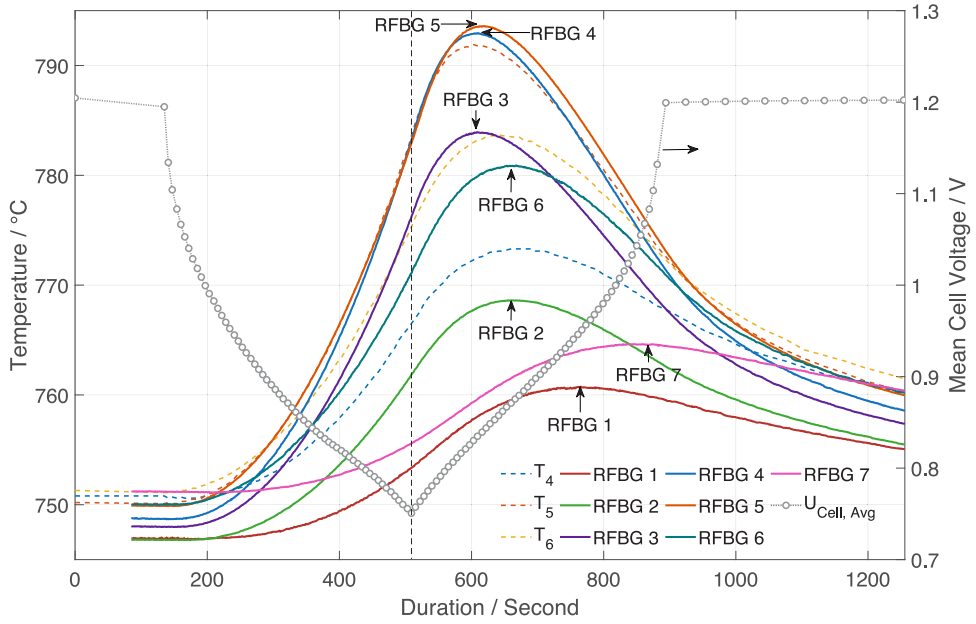

Fig. 5. Temperature development during polarization curve up to 120 A with 5.56 L min^{-1} H_2 and 20.00 L min^{-1} air, starting from about 750 °C.

important to note, however, that due to the limited spatial resolution and non-uniform thermal conductivity of different stack components, the resulting gradient profile is intended for qualitative analysis only. Overall, the thermal gradient inside this five layer short stack was primarily driven by the delayed heating of the bottom cover plate. To mitigate this gradient, the heating of the bottom and top cover plates should be synchronized by taking the thermal inertia of the adapter plate into consideration.

3.3. Temperature development during polarization measurement

The temperatures and the average cell voltage of the stack during the recording of a polarization curve are shown in Fig. 5. For clarity, only the temperatures measured by the thermocouples in the middle interconnect (T_4, T_5 and T_6) are included in this chart.

Prior to the measurement, the heating plates were set to 757 °C and T_5 stabilized at 750 °C. Once the current began to increase, the temperatures of all sensors started to rise due to the exothermic reaction. With a current ramp rate of 20 A per minute up to a maximum of 120 A in fuel cell mode, even though only the first half of the polarization curve data (current was ascending) was used for evaluation, the central stack temperature T_5 rose by approximately 35 °C at the peak current. This significant temperature elevation of the stack had substantial impact on the estimated area specific resistance (ASR) of the cells. In addition, this variation depends strongly on the test rig layout and stack design. Differences in thermal insulation, oven configuration and stack structure can lead to vastly different temperature profiles during the measurement, making the comparison of current voltage characteristics of different stacks very difficult. One potential way to mitigate the temperature variation during the polarization is to employ a much higher current ramp rate, which could reduce the influences from the aforementioned factors.

At around 600 s, while the current already started to decrease, T_5, RFBG 3, 4 and 5 reached their peak temperatures almost simultaneously, with the highest temperature of 793.5 °C being recorded by RFBG 5. For other temperature sensors, the time at which the temperatures peaked varied depending on their positions. As can be seen in the chart, RFBG 1 and 7 exhibited the largest degree of time shift, as they

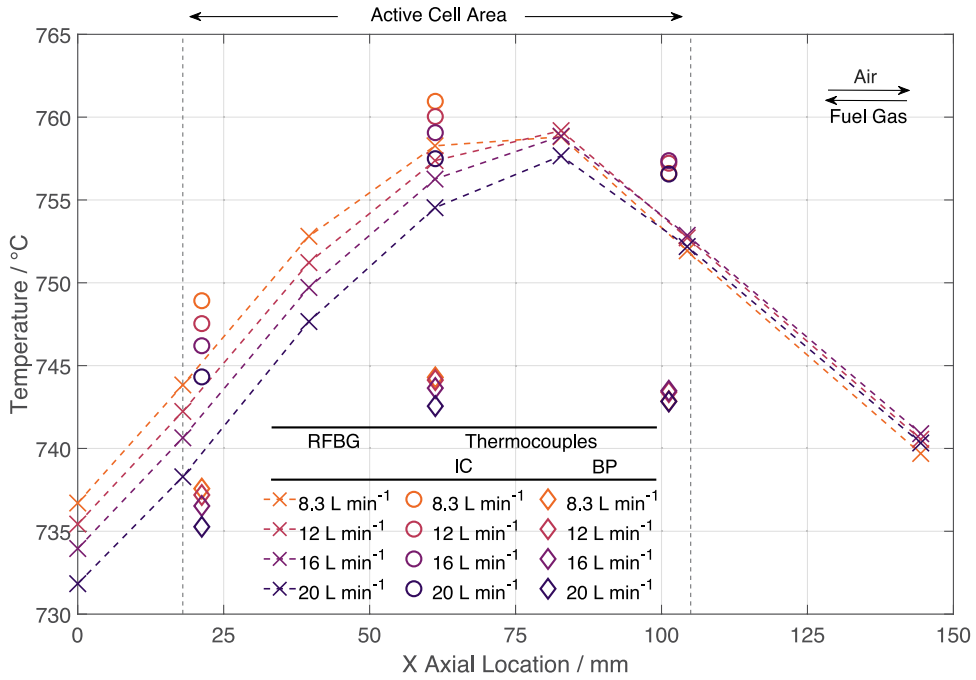

Fig. 6. Temperature distribution at different air flow rates during fuel cell operation at 60 A with 3.50 L min^{-1} H_2. Crosses: Temperatures measured by RFBG sensors 1 to 7; Circles: Temperatures measured by thermocouples 4, 5, 6 in the middle interconnect (IC); Diamonds: Temperatures measured by thermocouples 7, 8, 9 in the bottom cover plate (BP).

were placed outside of the reaction zone. RFBG 2 and 6, positioned at the edges of the reaction zone, displayed similar time shift, and so did the thermocouples T_4 and T_6. By analyzing these data acquired during the polarization curve, it should be possible to qualitatively identify the region with the highest current density and the relative distances from the sensors to the most reactive zone. However, further studies are required to fully exploit the high spatial resolution potential of RFBG sensors. Additionally, the temperature differences between the sensor pairs listed in Table 1 varied during the recording of the current voltage characteristics. Given that this measurement was performed at a relatively moderate current increment, it is expected that a larger difference between the readings of these sensor pairs would emerge as a result of more dynamic operation (e.g. quickly change the loading, gas supply failure etc.). Due to the inherent heat capacity of the interconnect, monitoring the transient temperature profile using only the thermocouples placed in interconnect might not be sufficient to capture these rapid yet critical changes.

The thermal gradient profile at 600 s is depicted in Fig. 4(b). Compared to the heat-up process, the thermocouples and RFBG sensors in the middle interconnect measured higher temperatures among all sensors and the arrows pointed towards the middle layer. At the left and right edges of the active zone, the gradient arrows displayed similar horizontal components directed towards the center. This behavior can be attributed to the cooling effect of air and fuel gas and the heat dissipation from the reaction zone.

3.4. Steady state fuel cell operation with varying air flow rate

To investigate the cooling effect of air flow on the temperature distribution in the stack, the stack was operated under steady state fuel cell mode with a current of 60 A (0.75 A cm^{-2}), 3.50 L min^{-1} of pure H_2 and varying air flow rates. The heating plate temperatures were maintained at 707 °C, so that the average temperature of nine thermocouples was about 700 °C at open circuit condition. The only variable parameter throughout these measurements was the air flow rate. The results are presented in Fig. 6.

The temperatures were recorded only after there was visually no change in the readings of all thermocouples and an arithmetic average of ten consecutive readings was calculated under each condition for all sensors. For the fiber-optic sensors, the temperature increased progressively from RFBG 1 to RFBG 5 and the highest temperature was consistently observed at RFBG 5 under all four different flow rates. Then the temperature decreased from RFBG 5 to 7, which can be attributed to the combined effect of lower fuel gas temperature and heat loss to the lateral wall of the stack. At the same x axial location, the thermocouples in interconnect and bottom cover plate measured an approximately 10 K to 15 K difference in temperature. Although increasing the air flow rate led to a subtle reduction in temperature across all sensors, the cooling effect was not proportional to the increase in air flow, especially at the air outlet side. At the air outlet manifold, RFBG 7 only recorded a 1.18 K difference between the 8.3 and 20 L min^{-1} air flow rate. This result is seemingly counter-intuitive, as a more pronounced influence of the air flow rate on the temperature distribution in the stack is generally expected, considering that excess air is typically used for cooling and mitigation of thermal gradient in the SOFC stacks [20,43]. To better understand this phenomenon, the energy balance of the stack should be analyzed. The heat production $\dot{Q}_{stack}$ of this five-layer stack under the defined operating condition can be expressed as:

$$\dot{Q}_{stack} = n \cdot (E^H - U_{Avg}) \cdot I \tag{3}$$

where E^H represents the thermoneutral voltage, n the number of stack layers, U_{Avg} the average cell voltage of the stack, I the current. Thermoneutral voltage is the potential difference across an electrochemical cell, at which the global electrochemical reaction neither produces nor consumes heat. For a general electrochemical reaction, it can be calculated as:

$$E^H = \frac{|\sum_i \nu_i \cdot H^\circ_{f,i}|}{nF} \tag{4}$$

ν_i denotes the stoichiometric coefficient of species i, $H^\circ_{f,i}$ the standard enthalpy of formation of species i at the given temperature, n the number of charges transferred, and F the Faraday constant. At 8.30 L min^{-1} and 20.00 L min^{-1} of air flow, U_{Avg} was 855 mV and 860 mV, and Eq. (3) yields 128.5 W and 127.1 W, respectively. Assuming that the air flow rate and composition did not change due to the oxygen

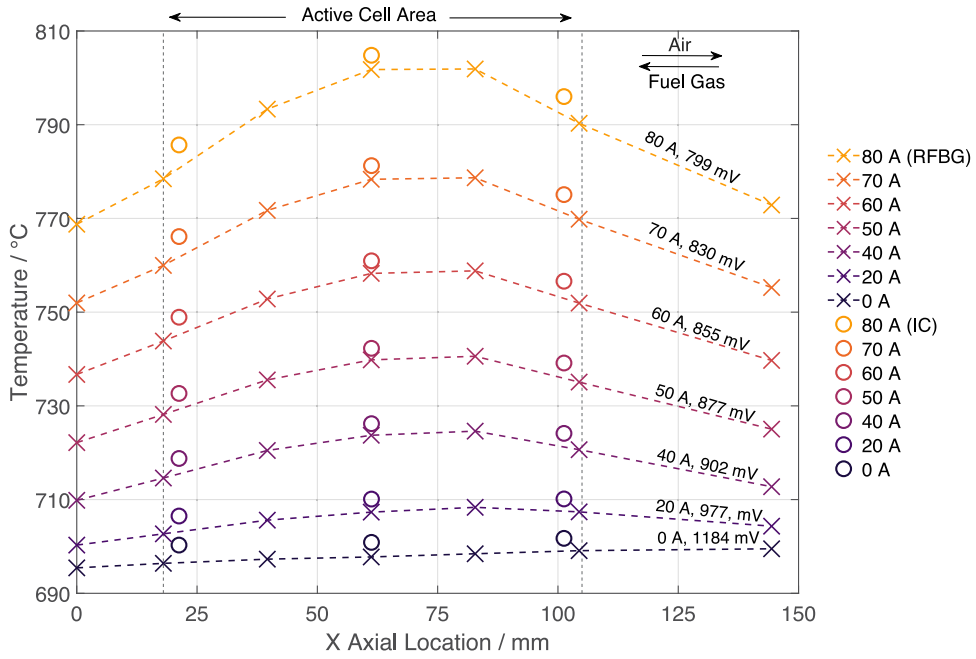

Fig. 7. Temperature distribution of the stack operated under different loads. The voltage value given was the average cell voltage at each current setpoint. Crosses: Temperatures measured by RFBG sensors; Circles: Temperatures measured by thermocouples in the middle interconnect (IC).

reduction reaction and the air entered the stack at 700 °C and left the stack at the temperature of air outlet manifold (measured by RFBG 7), the cooling power $\dot{Q}_{air}$ can be simplified as:

$$\dot{Q}_{air} = c_p \cdot \dot{m} \cdot (T_{out} - T_{in}) \quad (5)$$

c_p is the mass specific isobaric heat capacity of air at 700 °C, $\dot{m}$ the mass flow rate of the air, and T_{out} and T_{in} the temperatures of the air entered and left the stack. Applying this formula yields 8.1 W and 19.6 W at 8.30 and 20.00 L min^{-1} air, respectively.

The cooling power resulting from the temperature increase of the fuel gas can be estimated similarly. However, the heat capacity of the fuel gas cannot be assumed constant, given the 60% fuel gas utilization at 60 A. For a rough estimation, the heat capacity of the fuel gas mixture at 30% utilization and a temperature increase of 40 K (similar to air) are used, yielding 3.5 W. This analysis indicates that only 6.3% to 15.4% of the heat produced during fuel cell operation was removed through the convective air cooling in the stack, with even less removed by the fuel gas. Thus, in this five-layer short stack, the majority of the heat was dissipated to the surroundings through alternative pathways. The thermal gradient profile with 20.00 L min^{-1} air flow in Fig. 4(c) also supports this observation, as significant vertical thermal gradients were formed at the bottom and the top cover plates, indicating large heat loss in the vertical directions. In contrast, horizontal thermal gradients were primarily present near the region of air inlet as a consequence of convective cooling. The sources of the heat loss will be further articulated in the next section.

Regarding the stack operating strategy, the findings above suggest that using excess air for mitigation of temperature gradient in the SOC stack might not be an effective approach. First, in this five-layer stack, the temperature at the air outlet side barely changes with increasing air flow rate. Excess air could lower the temperature at the air inlet region while having minimal impact on the temperature of other regions, an effect is likely to be more pronounced in a larger stack. Second, higher flow rate increases the pressure drop in the air compartment, leading to greater energy consumption and making it more difficult to minimize the pressure difference between the fuel and air compartments. Finally, the energy required to preheat the air near the stack operating temperature can be substantial, which further reduces the overall system efficiency. An alternative approach to improve thermal management is optimizing the current stack design. For instance, Gong et al. [44] proposed a rotary L-type flow field design that can significantly diminish the temperature inhomogeneity during fuel cell operation compared to the counter flow configuration according to the simulation.

3.5. Steady state fuel cell operation with varying load

The temperature profiles of the stack operating under different loads during steady state fuel cell operation are compared in Fig. 7. With no load applied, the air temperature measured by RFBG 1 was 695.6 °C before entering the active cell area and 699.7 °C in the outlet manifold as recorded by RFBG 7. Once the load was applied, the temperature profile elevated progressively with the increasing current. At 80 A, in the middle of the active cell area, the temperature was 804.8 °C according to T_5 and 801.8 °C by RFBG 4. It is noteworthy that the RFBG sensors used in the present work were only calibrated up to 700 °C. Nevertheless, the close agreement between these sensors even up to 800 °C testified the strong potential of RFBG sensors for high temperature application. Compared to the OCV reference state, the temperatures measured by RFBG 4, 5 and thermocouple T_5 all increased by about 103 °C, while RFBG 1 and 7, located outside of the active cell area, recorded a temperature increase of 73 °C. Comparable temperature distributions were also reported for larger SOC stacks manufactured by Forschungszentrum Jülich [20] and in the simulation work of Russner et al. [45]. In contrast, the temperature increases measured by RFBG 1 and 7 during polarization curve barely exceeded 13 °C, as shown in Fig. 5. This difference can be ascribed to the thermal inertia of the stack components and the adapter plate. During the steady state operation, sufficient time was available to fully heat the whole stack and the adapter plate, which, in turn, enhanced the preheating of the air and fuel gas while passing through the adapter plate.

The thermal gradient at 80 A is illustrated in Fig. 4(d). In comparison to the profiles in Fig. 4(a) and (b), which were obtained during the heat-up process and polarization curve, the temperature gradient at the bottom cover plate was more pronounced than at the top cover plate. While operating at 80 A, the temperature setpoint for both heating plates was at 707 °C. However, the upper heating plate reached 772 °C without heating power due to the absence of convective cooling by

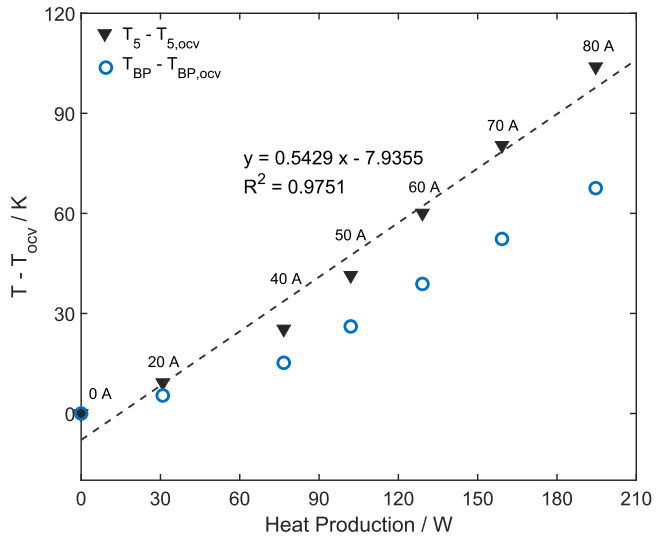

Fig. 8. Temperature differences of T_5 and average temperature of bottom cover plate (BP) regarding their reference values at OCV versus heat production of the stack during steady state fuel cell operation under different loads between 0 A and 80 A.

the air and the fuel gas. The thick thermal insulation surrounding both the stack and the heating plate minimized the heat loss from the top cover plate, resulting in a relatively small thermal gradient. For the lower heating plate, due to the presence of the air and fuel gas flow, the temperature remained at the setpoint during operation. Consequently, a considerable temperature difference emerged between the lower heating plate and the bottom cover plate, causing a higher heat loss in the lower part of the stack.

Fig. 8 shows the correlations of the temperature elevations compared to their respective values at OCV conditions with the total heat production of the stack. The heat production can be calculated using Eq. (3), and the thermoneutral voltage at 750 °C, 1285.2 mV, was selected due to T_5 ranging from 700 °C to 800 °C. The cell voltages at each corresponding current can be found in supplementary material S2. A linear fit for $T_5 - T_{5,ocv}$ and heat production, shown as the dashed line in the chart, yields an R^2 value of 0.9751, suggesting a satisfactory degree of linear correlation. The temperature of bottom cover plate T_{BP}, averaged from T_7, T_8 and T_9, also showed a similar tendency yet with a less steep slope. The energy balance of the stack must be considered to clarify the cause of this linear behavior. Assuming that T_5 was the hottest spot in the stack, the heat loss through thermal insulation and the cooling effect contributed by fuel gas were negligible:

$$\dot{Q}_{stack} = \dot{Q}_{air} + \frac{T_5 - T_{\text{lower heating plate}}}{R_{th,1}} + \frac{T_5 - T_{\text{upper heating plate}}}{R_{th,2}} \tag{6}$$

where $R_{th,1}$ is the thermal resistance between the thermocouple T_5 and the lower heating plate, $R_{th,2}$ the thermal resistance between the thermocouple T_5 and the upper heating plate. The thermal resistance in Eq. (6) is a serial combination of multiple conductive and thermal radiation terms:

$$R_{th} = \sum_i R_{\text{conductive},\ i} + \sum_j R_{\text{radiation},\ j} \tag{7}$$

As discussed in the previous section, convective air cooling accounts for only a small portion of the heat dissipation during fuel cell operation. Given the more prominent thermal gradient in the BP, it is reasonable to assume that most of the heat was dissipated to the lower heating plate through the BP. Thus, Eq. (6) could be simplified as follows:

$$\dot{Q}_{stack} = \frac{T_5 - T_{\text{lower heating plate}}}{R_{\text{conductive}} + R_{\text{radiative}}} \tag{8}$$

While it is challenging to analytically determine the thermal resistance from the hot spot of the stack to the lower heating plate, the linearity observed between the temperature elevation and the heat production hinted at a nearly constant value of thermal resistance, regardless of the T_5 and the temperature of BP. The conductive terms are defined by the material properties and stack construction, which are not strongly temperature dependent. The heat transfer between the bottom cover plate and the adapter plate occurred primarily via thermal radiation, which can be approximated as radiative heat transfer between two infinite parallel surfaces, which can be approximated using the Stefan–Boltzmann law for thermal radiation between two infinite parallel surfaces [46]:

$$\frac{\dot{q}}{A} = \frac{\sigma(T_1^4 - T_2^4)}{\varepsilon_1^{-1} + \varepsilon_2^{-1} - 1} \tag{9}$$

where $\dot{q}$ denotes the total heat flow rate, A the area of the surface, σ the Stefan–Boltzmann constant, T_1 and T_2 the temperatures of the adjacent surfaces in Kelvin, ε_1 and ε_2 the mean emissivities of the surface 1 and 2. It is evident that the heat flow contributed by radiation should drastically increase with the rising bottom cover plate temperature because of the T^4 dependence. However, this was not reflected in Fig. 8. This suggests that the thermal radiation did not have a considerable contribution to the thermal resistance for this five layer F10 stack and heat conduction should be the rate determining step. In addition, it is noteworthy that the data up to 40 A slightly deviated from the fitted line with a smaller slope, suggesting an increase in total thermal resistance as the stack temperature increased. One possible explanation is the decrease in thermal conductivity of the Crofer 22 APU material with increasing temperature within this temperature range [47].

4. Conclusions

In this work, a five-layer F10 SOC stack was modified to incorporate an optical fiber equipped with an array of seven regenerated fiber Bragg grating (RFBG) sensors. The installation of the fiber and the modification of the stack had no impact on the overall electrochemical performance of the stack and the stack layer, where the fiber and the guiding tube was placed on. To complement the optical fiber sensors, nine carefully inspected type-N thermocouples were employed to validate the RFBG sensors and to provide additional temperature measurements across other stack layers under both transient and steady state operating conditions. The RFBG sensors demonstrated high temperature resistance and fidelity up to 800 °C, while the non electrical conductive nature and chemically inertness of silica in dry air ensured the safe employment of the optical fiber in the SOC stack. The compact size and multiplexing capability of this sensor provided a new avenue to study the temperature distribution directly inside the stack, an area hardly accessible to conventional thermocouples. This work revealed the potential issue of asynchronous heating of the stack, which led to a temperature gradient inside the short stack during the heat-up process. Furthermore, the standard procedure to perform polarization curve at Forschungszentrum Jülich is based on a current ramp rate of 20 A min^{-1}, which can cause significant temperature elevation inside the stack during the characterization and introduce bias to the assessment of stack performance. Moreover, the RFBG sensors might be more suitable for measurement of transient temperature variation than the thermocouples, since they can be placed much closer to the active cell area. The effect of air flow on the temperature profile was studied at a fixed current setpoint and varying air flow rates during fuel cell operation. The increasing air flow indeed reduced the thermal gradient and hot spot but only to a very limited extent. An analysis of the energy balance revealed that the convective air cooling in the short stack did not play a significant role in removing the heat generated during fuel cell operation in this setup. Finally, the temperature profiles of the stack operated at different electrical power outputs were compared and an adequate linearity was found between the temperature increase in T_5

relative to the OCV state and the total heat production of the stack, suggesting that heat conduction, rather than thermal radiation, should be the rate determining step for heat dissipation of the stack.

In sum, this work demonstrated the potential of RFBG sensors as an alternative temperature sensing technique for solid oxide cell stack application. Future studies should aim to address the issue of inhomogeneous temperature distribution during heat-up phase, and further investigate how varying current ramp rates impact the estimation of ASR value. Moreover, this sensing technique could also be extended to other stack design, e.g. Jülich H20 stack, to support the optimization of operating strategy.

CRediT authorship contribution statement

Shengzhi Liang: Writing – original draft, Visualization, Investigation, Data curation, Conceptualization, Writing – review & editing. **Qiang Bian:** Resources, Investigation, Writing – review & editing. **Dominik Schäfer:** Supervision, Project administration, Conceptualization, Writing – review & editing. **Johannes Roths:** Resources, Writing – review & editing. **Rüdiger-A. Eichel:** Supervision.

Declaration of competing interest

The authors declare that they have no known competing financial interests or personal relationships that could have appeared to influence the work reported in this paper.

Acknowledgments

The Helmholtz Society and the German Federal Ministry of Education and Research are gratefully acknowledged for financing these activities as part of the iNEW 2.0 project (03SF0627A). The authors acknowledge all colleagues from Photonics laboratory, Munich University of Applied Sciences for supplying the RFBG sensors used in this work and the support. Special thanks go to Arnold Cramer (Institute of Technology and Engineering, Forschungszentrum Jülich GmbH) for the preparation of the stack, Rabah Lekehal and Stefan Küpper (Institute of Energy Technologies, Forschungszentrum Jülich GmbH) for their technical support and preparation of the test rig, and Dr. Remzi Can Samsun for the valuable suggestions on the manuscript.

Appendix A. Supplementary data

Supplementary material related to this article can be found online at https://doi.org/10.1016/j.jpowsour.2025.237120.

Data availability

Data will be made available on request.

References

[1] D. Udomsilp, C. Lenser, O. Guillon, N.H. Menzler, Performance benchmark of planar solid oxide cells based on material development and designs, Energy Technol. 9 (4) (2021) 2001062, http://dx.doi.org/10.1002/ente.202001062.

[2] S. Zarabi Golkhatmi, M.I. Asghar, P.D. Lund, A review on solid oxide fuel cell durability: Latest progress, mechanisms, and study tools, Renew. Sustain. Energy Rev. 161 (2022) 112339, http://dx.doi.org/10.1016/j.rser.2022.112339.

[3] V. Subotić, C. Hochenauer, Analysis of solid oxide fuel and electrolysis cells operated in a real-system environment: State-of-the-health diagnostic, failure modes, degradation mitigation and performance regeneration, Prog. Energy Combust. Sci. 93 (2022) 101011, http://dx.doi.org/10.1016/j.pecs.2022.101011.

[4] A. Stambouli, E. Traversa, Solid oxide fuel cells (sofcs): a review of an environmentally clean and efficient source of energy, Renew. Sustain. Energy Rev. 6 (5) (2002) 433–455, http://dx.doi.org/10.1016/S1364-0321(02)00014-X.

[5] Q. Fang, U. de Haart, D. Schäfer, F. Thaler, V. Rangel-Hernandez, R. Peters, L. Blum, Degradation analysis of an sofc short stack subject to 10,000 h of operation, J. Electrochem. Soc. 167 (14) (2020) 144508, http://dx.doi.org/10.1149/1945-7111/abc843.

[6] U.S. Department of Energy, Report To Congress on the Status of the Solid Oxide Fuel Cell Program, Tech. Rep., Office of Fossil Energy and Carbon Management, U.S. Department of Energy, 2025, accessed Feb. 24 (2023).

[7] S.J. Kim, M.-B. Choi, M. Park, H. Kim, J.-W. Son, J.-H. Lee, B.-K. Kim, H.-W. Lee, S.-G. Kim, K.J. Yoon, Acceleration tests: Degradation of anode-supported planar solid oxide fuel cells at elevated operating temperatures, J. Power Sources 360 (2017) 284–293, http://dx.doi.org/10.1016/j.jpowsour.2017.06.004.

[8] M. Riegraf, K. Develos-Bagarinao, I. Biswas, R. Costa, The influence of sulfur impurities in industrial cox gases on solid oxide electrolysis cell (soec) degradation, J. Power Sources 559 (2023) 232669, http://dx.doi.org/10.1016/j.jpowsour.2023.232669.

[9] D. Schäfer, L. Queda, V. Nischwitz, Q. Fang, L. Blum, Origin of steam contaminants and degradation of solid-oxide electrolysis stacks, Processes 10 (3) (2022) 598, http://dx.doi.org/10.3390/pr10030598.

[10] M.B. Mogensen, M. Chen, H.L. Frandsen, C. Graves, A. Hauch, P.V. Hendriksen, T. Jacobsen, S.H. Jensen, T.L. Skafte, X. Sun, Ni migration in solid oxide cell electrodes: Review and revised hypothesis, Fuel Cells (2021) http://dx.doi.org/10.1002/fuce.202100072.

[11] J.-S. Shin, M. Saqib, M. Jo, K. Park, K.M. Park, J.S. Ahn, H.-T. Lim, J.-Y. Park, Degradation mechanisms of solid oxide fuel cells under various thermal cycling conditions, ACS Appl. Mater. Interfaces 13 (42) (2021) 49868–49878, http://dx.doi.org/10.1021/acsami.1c13779.

[12] Y. Yang, X. Tong, A. Hauch, X. Sun, Z. Yang, S. Peng, M. Chen, Study of solid oxide electrolysis cells operated in potentiostatic mode: Effect of operating temperature on durability, Chem. Eng. J. 417 (2021) 129260, http://dx.doi.org/10.1016/j.cej.2021.129260.

[13] N.H. Menzler, D. Sebold, Y.J. Sohn, S. Zischke, Post-test characterization of a solid oxide fuel cell after more than 10 years of stack testing, J. Power Sources 478 (2020) 228770, http://dx.doi.org/10.1016/j.jpowsour.2020.228770.

[14] L.G.J. de Haart, J. Mougin, O. Posdziech, J. Kiviaho, N.H. Menzler, Stack degradation in dependence of operation parameters; the real-sofc sensitivity analysis, Fuel Cells 9 (6) (2009) 794–804, http://dx.doi.org/10.1002/fuce.200800146.

[15] A. Nakajo, Z. Wuillemin, J. van Herle, D. Favrat, Simulation of thermal stresses in anode-supported solid oxide fuel cell stacks. part i: Probability of failure of the cells, J. Power Sources 193 (1) (2009) 203–215, http://dx.doi.org/10.1016/j.jpowsour.2008.12.050.

[16] A. Nakajo, Z. Wuillemin, J. van Herle, D. Favrat, Simulation of thermal stresses in anode-supported solid oxide fuel cell stacks. part ii: Loss of gas-tightness, electrical contact and thermal buckling, J. Power Sources 193 (1) (2009) 216–226, http://dx.doi.org/10.1016/j.jpowsour.2008.12.039.

[17] L.-K. Chiang, H.-C. Liu, Y.-H. Shiu, C.-H. Lee, R.-Y. Lee, Thermo-electrochemical and thermal stress analysis for an anode-supported sofc cell, Renew. Energy 33 (12) (2008) 2580–2588, http://dx.doi.org/10.1016/j.renene.2008.02.023.

[18] O. Razbani, I. Wærnhus, M. Assadi, Experimental investigation of temperature distribution over a planar solid oxide fuel cell, Appl. Energy 105 (2013) 155–160, http://dx.doi.org/10.1016/j.apenergy.2012.12.062.

[19] S. Celik, B. Timurkutluk, M.D. Mat, Measurement of the temperature distribution in a large solid oxide fuel cell short stack, Int. J. Hydrog. Energy 38 (25) (2013) 10534–10541, http://dx.doi.org/10.1016/j.ijhydene.2013.06.024.

[20] Q. Fang, L. Blum, P. Batfalsky, N.H. Menzler, U. Packbier, D. Stolten, Durability test and degradation behavior of a 2.5 kw sofc stack with internal reforming of lng, Int. J. Hydrog. Energy 38 (36) (2013) 16344–16353, http://dx.doi.org/10.1016/j.ijhydene.2013.09.140.

[21] H. Cheng, X. Li, J. Jiang, Z. Deng, J. Yang, J. Li, A nonlinear sliding mode observer for the estimation of temperature distribution in a planar solid oxide fuel cell, Int. J. Hydrog. Energy 40 (1) (2015) 593–606, http://dx.doi.org/10.1016/j.ijhydene.2014.10.117.

[22] M. Ranaweera, J.-S. Kim, Cell integrated multi-junction thermocouple array for solid oxide fuel cell temperature sensing: N+1 architecture, J. Power Sources 315 (2016) 70–78, http://dx.doi.org/10.1016/j.jpowsour.2016.03.002.

[23] E. Guk, J.-S. Kim, M. Ranaweera, V. Venkatesan, L. Jackson, In-situ monitoring of temperature distribution in operating solid oxide fuel cell cathode using proprietary sensory techniques versus commercial thermocouples, Appl. Energy 230 (2018) 551–562, http://dx.doi.org/10.1016/j.apenergy.2018.08.120.

[24] E. Guk, V. Venkatesan, S. Babar, L. Jackson, J.-S. Kim, Parameters and their impacts on the temperature distribution and thermal gradient of solid oxide fuel cell, Appl. Energy 241 (2019) 164–173, http://dx.doi.org/10.1016/j.apenergy.2019.03.034.

[25] E. Guk, M. Ranaweera, V. Venkatesan, J.-S. Kim, Performance and durability of thin film thermocouple array on a porous electrode, Sensors (Basel, Switz.) 16 (9) (2016) http://dx.doi.org/10.3390/s16091329.

[26] D. Brett, P. Aguiar, R. Clague, A.J. Marquis, S. Schöttl, R. Simpson, N.P. Brandon, Application of infrared thermal imaging to the study of pellet solid oxide fuel cells, J. Power Sources 166 (1) (2007) 112–119, http://dx.doi.org/10.1016/j.jpowsour.2006.12.098.

[27] R. Montanini, A. Quattrocchi, S.A. Piccolo, A. Amato, S. Trocino, S.C. Zignani, M. Lo Faro, G. Squadrito, Real-time thermal imaging of solid oxide fuel cell cathode activity in working condition, Appl. Opt. 55 (25) (2016) 7142–7148, http://dx.doi.org/10.1364/AO.55.007142.

[28] J.B. Robinson, L.D. Brown, R. Jervis, O.O. Taiwo, T.M. Heenan, J. Millichamp, T.J. Mason, T.P. Neville, R. Clague, D.S. Eastwood, C. Reinhard, P.D. Lee, D.J. Brett, P.R. Shearing, Investigating the effect of thermal gradients on stress in solid oxide fuel cell anodes using combined synchrotron radiation and thermal imaging, J. Power Sources 288 (2015) 473–481, http://dx.doi.org/10.1016/j.jpowsour.2015.04.104.

[29] S. Ma, Y. Xu, Y. Pang, X. Zhao, Y. Li, Z. Qin, Z. Liu, P. Lu, X. Bao, Optical fiber sensors for high-temperature monitoring: A review, Sensors (Basel, Switz.) 22 (15) (2022) http://dx.doi.org/10.3390/s22155722.

[30] J. Wu, M. Wang, K. Zhao, S. Huang, M. Zaghloul, R. Cao, D. Carpenter, G. Zheng, S. Rountree, K.P. Chen, Distributed fiber sensors with high spatial resolution in extreme radiation environments in nuclear reactor cores, J. Lightwave Technol. 39 (14) (2021) 4873–4883, http://dx.doi.org/10.1109/JLT.2021.3075630.

[31] A. Yan, S. Huang, S. Li, R. Chen, P. Ohodnicki, M. Buric, S. Lee, M.-J. Li, K.P. Chen, Distributed optical fiber sensors with ultrafast laser enhanced rayleigh backscattering profiles for real-time monitoring of solid oxide fuel cell operations, Sci. Rep. 7 (1) (2017) 9360, http://dx.doi.org/10.1038/s41598-017-09934-3.

[32] L. Polz, F.J. Dutz, R.R. Maier, H. Bartelt, J. Roths, Regenerated fibre bragg gratings: A critical assessment of more than 20 years of investigations, Opt. Laser Technol. 134 (2021) 106650, http://dx.doi.org/10.1016/j.optlastec.2020.106650.

[33] F. Buchfellner, A. Stadler, Q. Bian, M. Hennesen, A. Zeisberger, A.W. Koch, J. Roths, Generalized and wavelength-dependent temperature calibration function for multipoint regenerated fiber bragg grating sensors, Opt. Express 30 (25) (2022) 44769–44784, http://dx.doi.org/10.1364/OE.470093.

[34] Y.-J. Rao, In-fibre bragg grating sensors, Meas. Sci. Technol. 8 (4) (1997) 355–375, http://dx.doi.org/10.1088/0957-0233/8/4/002.

[35] G. Laffont, R. Cotillard, P. Ferdinand, Multiplexed regenerated fiber bragg gratings for high-temperature measurement, Meas. Sci. Technol. 24 (9) (2013) 094010, http://dx.doi.org/10.1088/0957-0233/24/9/094010.

[36] M. Lindner, E. Tunc, K. Weraneck, F. Heilmeier, W. Volk, M. Jakobi, A.W. Koch, J. Roths, Regenerated bragg grating sensor array for temperature measurements during an aluminum casting process, IEEE Sensors J. 18 (13) (2018) 5352–5360, http://dx.doi.org/10.1109/JSEN.2018.2837164.

[37] F.J. Dutz, A. Heinrich, R. Bank, A.W. Koch, J. Roths, Fiber-optic multipoint sensor system with low drift for the long-term monitoring of high-temperature distributions in chemical reactors, Sensors (Basel, Switz.) 19 (24) (2019) http://dx.doi.org/10.3390/s19245476.

[38] Q. Bian, C. Bauer, A. Stadler, M. Lindner, M. Jakobi, W. Volk, A.W. Koch, J. Roths, In-situ high temperature and large strain monitoring during a copper casting process based on regenerated fiber bragg grating sensors, J. Lightwave Technol. 39 (20) (2021) 6660–6669, http://dx.doi.org/10.1109/JLT.2021.3101524.

[39] Q. Fang, L. Blum, N.H. Menzler, Performance and degradation of solid oxide electrolysis cells in stack, J. Electrochem. Soc. 162 (8) (2015) F907–F912, http://dx.doi.org/10.1149/2.0941508jes.

[40] Y. Yan, Q. Fang, L. Blum, W. Lehnert, Performance and degradation of an soec stack with different cell components, Electrochim. Acta 258 (2017) 1254–1261, http://dx.doi.org/10.1016/j.electacta.2017.11.180.

[41] Q. Fang, L. Blum, D. Stolten, Electrochemical performance and degradation analysis of an sofc short stack following operation of more than 100, 000 hours, J. Electrochem. Soc. 166 (16) (2019) F1320–F1325, http://dx.doi.org/10.1149/2.0751916jes.

[42] MathWorks, Gradient function - MATLAB, 2025, URL https://www.mathworks.com/help/matlab/ref/gradient.html. (Accessed 11 February 2025).

[43] Q. Fang, L. Blum, R. Peters, M. Peksen, P. Batfalsky, D. Stolten, Sofc stack performance under high fuel utilization, Int. J. Hydrog. Energy 40 (2) (2015) 1128–1136, http://dx.doi.org/10.1016/j.ijhydene.2014.11.094.

[44] C. Gong, Z. Tu, S. Hwa Chan, A novel flow field design with flow re-distribution for advanced thermal management in solid oxide fuel cell, Appl. Energy 331 (2023) 120364, http://dx.doi.org/10.1016/j.apenergy.2022.120364.

[45] N. Russner, S. Dierickx, A. Weber, R. Reimert, E. Ivers-Tiffée, Multiphysical modelling of planar solid oxide fuel cell stack layers, J. Power Sources 451 (2020) 227552, http://dx.doi.org/10.1016/j.jpowsour.2019.227552.

[46] J.P. Holman, Heat transfer, in: McGraw-Hill Series in Mechanical Engineering, 10th Edition, McGraw Hill Higher Education, Boston, 2010.

[47] VDM Metals International GmbH, Data sheet VDM crofer 22 APU, 2025, URL https://www.vdm-metals.com/fileadmin/user_upload/Downloads/Data_Sheets/Data_Sheet_VDM_Crofer_22_APU.pdf. (Accessed 08 April 2025).